CORA Cork Open Research Archive
Cartlann Taighde Oscailte Chorcaí

Title	An epidermal wearable microfluidic patch for simultaneous sampling, storage, and analysis of biofluids with counterion monitoring.
Authors	Kunnel, Brince P.;Demuru, Silvia
Publication date	2022-03-07
Original Citation	Kunnel, B. P. and Demuru, S. (2022) 'An epidermal wearable microfluidic patch for simultaneous sampling, storage, and analysis of biofluids with counterion monitoring', Lab on a Chip, (12 pp). doi: 10.1039/D2LC00183G
Type of publication	Article (peer-reviewed)
Link to publisher's version	https://pubs.rsc.org/en/content/articlelanding/2022/lc/d2lc00183g - 10.1039/d2lc00183g
Rights	© The Royal Society of Chemistry 2022
Download date	2026-11-04 05:00:56
Item downloaded from	https://hdl.handle.net/10468/13126

UCC
University College Cork, Ireland
Coláiste na hOllscoile Corcaigh

Check for updates

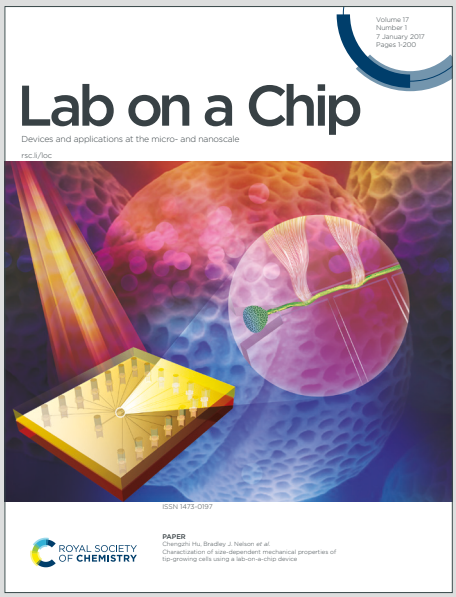
View Article Online
View Journal

Lab on a Chip

Devices and applications at the micro- and nanoscale

Accepted Manuscript

This article can be cited before page numbers have been issued, to do this please use: B. Paul Kunnel and S. Demuru, *Lab Chip*, 2022, DOI: 10.1039/D2LC00183G.



This is an Accepted Manuscript, which has been through the Royal Society of Chemistry peer review process and has been accepted for publication.

Accepted Manuscripts are published online shortly after acceptance, before technical editing, formatting and proof reading. Using this free service, authors can make their results available to the community, in citable form, before we publish the edited article. We will replace this Accepted Manuscript with the edited and formatted Advance Article as soon as it is available.

You can find more information about Accepted Manuscripts in the Information for Authors.

Please note that technical editing may introduce minor changes to the text and/or graphics, which may alter content. The journal's standard Terms & Conditions and the Ethical guidelines still apply. In no event shall the Royal Society of Chemistry be held responsible for any errors or omissions in this Accepted Manuscript or any consequences arising from the use of any information it contains.

ROYAL SOCIETY OF CHEMISTRY

rsc.li/loc

View Article Online
DOI: 10.1039/D2LC00183G

ARTICLE

An epidermal wearable microfluidic patch for simultaneous sampling, storage, and analysis of biofluids with counterions monitoring

Received 00th January 20xx,
Accepted 00th January 20xx

DOI: 10.1039/x0xx00000x

Brince Paul Kunnel,*[ab] and Silvia Demuru [a]

Simultaneous access to the different biofluids enables an accurate analysis of multiple analytes, leading to a precision diagnosis and medication. Additionally, establishing a relationship between various markers at different biofluids and their correlation to blood allows developing an algorithmic approach, which aids non-invasive diagnosis through single parameter monitoring. However, the main bottleneck that exists in multiple biofluid analyses for its clinical implementation is the requirements of the advanced microfluidic coupled device design, which empowers simultaneous collection and monitoring. To tackle this challenge, we present an epidermal wearable bio-fluidics patch that facilitates simultaneous on-demand extraction, sampling, and storage of sweat and interstitial fluid (ISF) along with monitoring of their corresponding counterions. The clean room-free development of biofluidic patch is realized through 3-D integration of laser patterned optimized microfluidics structures, low-cost screen-printed stimulation module, and potentiometric chloride (Cl^-) and calcium (Ca^{2+}) ions sensing module for adequate dual biofluid sampling and analysis. The developed Cl^- and Ca^{2+} ion-selective sensors exhibit good repeatability, selectivity, acceptable stability, and sensitivity. The proof of concept demonstration of the fabricated patch for simultaneous dual-sampling, storage, and monitoring of the sweat Cl^- and ISF Ca^{2+} on a healthy volunteer during different day periods leverages its potential in real-time personalized healthcare clinical usages. Further, the patch's feasibility in electronic interface and wireless transmission facilitates point-of-care non-invasive lab-on-skin application for monitoring the health status of individuals.

Introduction

Internet of things has revolutionized medical diagnostics with the concept of telemedicine and e-health, especially in the field of electrophysiological signal monitoring such as electrocardiography, electromyography, and electroencephalography.[1-5] However, the complexity in bulk sensor acquisition systems and the requirement of the skilled operators has led to the exploration of advanced flexible and skin interfaceable sensors that not only resulted in wearable electrophysiological signal acquisition devices such as smartwatches but wearable haptics based biorobots for fitness and health monitoring.[2-8] Compared to the substantial advancement in physical data acquisition, molecular health diagnosis still hinges on conventional invasive blood or urine grounded analysis, which requires specialists for sampling, measuring, and interpreting the data.[9] Even if some flourished efforts have been made to explore analytes from tear, sweat, and saliva as an alternative to the blood, simultaneous probing of different biofluids and establishing the reliable relationships among the analytes could facilitate precision diagnostics.[9,10]

In recent years, sweat, an epidermal biofluid excreted by the eccrine sweat gland, has been explored widely for healthcare applications due to the presence of rich biochemical analytes such as proteins, ions, nutrients, and metabolites.[11] As several of these markers circulates from blood, sweat analysis can be an alternative to track the individual's health information.[12] There have been numerous efforts to manufacture wearable sweat epidermal platforms for multiplexed monitoring of electrolytes, metabolites, and proteins based on different sensing mechanisms.[13-17] Among them, electrochemical sensors facilitate versatile, cost-effective, and easy interfacing through wearable technology.[18] Based on sweat analysis, it is possible to effectively monitor the various health conditions such as cystic fibrosis, metabolic alkalosis, diabetes, nutrition deficiency, and body dehydration. [18-26] Interestingly, some reports have shown the successful correlation of sweat lactate and ethanol with blood.[22,27] Although most epidermal sweat sensors exploit sweat generation through prolonged exercise, the iontophoresis process has been established for on-demand sweat induction, especially for infants, sedentary individuals, and elders. [28-36] Thus, devotion to developing the sweat-based sensors and exploration of in-situ analysis of different sweat analytes and their correlation affords great promise for future non-invasive clinical diagnostics.

ISF is another attractive body fluid that resides in the interstitial space amongst cells, and many of the ISF markers migrate from the bloodstream.[38] Several ISF analytes have shown a good correlation with corresponding blood components by providing great promises as a biofluid for diagnosis.[35] The primary challenge that exists is the epidermal extraction of the ISF: even though ultrasonic-based sonophoresis has been shown as a potential technique for

[a] Soft Transducers Laboratory, École Polytechnique Fédérale de Lausanne (EPFL), 2000 Neuchatel, Switzerland.
[b] Micro and Nano systems Centre, Tyndall National Institute, T12 R5CP Cork, Ireland. Email :brince.kunnel@tyndall.ie.

Electronic Supplementary Information (ESI) available: [details of any supplementary information available should be included here]. See DOI: 10.1039/x0xx00000x

Published on 07 March 2022. Downloaded by University College Cork on 3/8/2022 3:24:05 PM.

Lab on a Chip Accepted Manuscript

View Article Online
DOI: 10.1039/D1LC01104J

Published on 07 March 2022. Downloaded by University College Cork on 3/8/2022 3:24:05 PM.

extraction, it is complex to integrate it into wearable devices.[39,40] Alternatively, microneedle array-based transdermal devices can be used to access the ISF through skin penetration and have been demonstrated for sensing glucose, potassium (K^+), sodium (Na^+) ions, and proteins.[37,41] However, the main complications lie in the fabrication of microneedles, the possible delamination of the sensor's surface during insertion, and toxicity due to the direct interaction of sensor constituents such as ionophores with ISF. Reverse iontophoresis, which involves delivering mild current across the epidermis, has emerged as another method to extract ISF and molecules present in it.[42] Some progressive development has been made to extract ions and metabolites from ISF based on this principle. Christopher et al. demonstrated successful quantification of glucose and potassium transdermally extracted into a gel using reverse iontophoresis.[43] Benoit et al. showed therapeutic drug monitoring application by reverse iontophoretically extracting phenytoin and successfully correlated with its subdermal concentration.[44] Yao et al. reported integrating an ISF extraction module and glucose sensors in a single device.[45] Also, Bandodkar et al. successfully demonstrated advanced manufacturing of wearable tattoo-based glucose monitoring for extracting ISF using reverse iontophoresis.[35] Tierney et al. has shown accurate tracking of transcutaneously extracted glucose with blood glucose for a non-diabetic volunteer.[46] In another study, Yihao et al. reported a paper battery-powered skin-like glucose biosensor for ISF glucose monitoring and showed a good correlation with clinically examined blood glucose.[47] Interestingly, in a recent study on extended interstitial fluid glucose monitoring, Ernesto et al. demonstrated successful decoding of ISF and validated the good correlation of ISF glucose with blood glucose levels for diabetic and non-diabetic patients.[48] All these studies show the feasibility of the reverse iontophoresis method for ISF extraction and ease implementation into wearables compared to microneedles and ultrasonic-based sampling.

Despite numerous reports of wearable epidermal sensors demonstrated for separate biofluid analysis, there are not many efforts devoted to developing wearable sensors for simultaneous collection and investigation of various biofluids that lead to a precision diagnosis. The wearable sensor for simultaneous evaluation of body fluids such as urine, sweat, and tear have been demonstrated by ex-situ analysis.[49] The studies on wearable tattoo platforms for simultaneous monitoring of sweat-alcohol and ISF-glucose and the recent demonstration on simultaneous analysis of metabolites and hemodynamic parameters have shown some progressive effort in this field.[50,51] However, there exist some complications to implementing this in practical application, such as (i) possibility of delamination and contamination of the sensor's functionalization materials due to direct contact of sensing layer coated surfaces to the skin causes, (ii) the evaporation of biofluid causing unstable sensors readings due to integration of the extraction and sensing modules into a single layer, and the (iii) probability of mixing of the distinct biofluids extracted simultaneously to the skin surface during a long time operation (by occurring the flow of extracted fluids through the skin surface due to lack of different collection chambers whenever secretion begins). These challenges can be addressed by implementing a layered structure of the intelligent and optimized fluidic sensing patch that facilitates separate but simultaneous sampling of biofluids to analyze corresponding analytes. The interfacing of the appropriate microfluidic features not only boosts the efficient biofluid collection by avoiding cross-talk but benefits future analysis of collected biosamples.[52,53]

Herein, we present a novel sweat and interstitial fluidics patch (SIFP) for on-demand simultaneous extraction, collection, analysis, and storage of biofluids. The SIFP uses the iontophoresis process at the anode and the reverse iontophoresis process at the cathode side of the patch for parallel extraction of sweat and ISF biofluids, respectively. The SIFP's ability for simultaneous collection of sweat and ISF enables establishing the relationship between these two biofluids at different physiological conditions as well as various markers present in them. Furthermore, finding a relationship between diverse analytes at different biofluids and their correlation to blood facilitates to establish non-invasive precision diagnosis through single parameter monitoring by an algorithmic approach. As an initial effort, the multiplexed monitoring of sweat Cl^- and ISF Ca^{2+} has been demonstrated for a proof of concept by embedding the respective ion-selective sensors in SIFP's fluid transport path. Cl^- ion is one of the important markers in sweat as its concentration level screens is used for screening cystic fibrosis (CF) patients [19]. Ca^{2+} in biological fluid plays an essential role in metabolism as well as minerals homeostasis.[49] Although there have been few reports on elevated intracellular Ca^{2+} concentration in CF cells, which might influence cellular metabolism, there have been no extensive studies to prove this concept due to the lack of simultaneous monitoring of CF and Ca^{2+} ions from the interstitial spaces.[54-57] The SIFP addresses similar challenges by providing an effective way of collecting sweat and ISF simultaneously and demonstrating its capability to monitor sweat Cl^- and ISF Ca^{2+} as model electrolytes. The cost-effective, cleanroom-free fabrication of SIFP is achieved by 3D integration of layered architectures of the laser engraved fluidics structures for efficient sampling and storage of bio-fluids and screen printing of ion-selective sensors followed by modification with the respective Ca^{2+} and Cl^- selective membranes. The concept of continuous collection and withdrawal of collected biofluids in SIFP fluidics is also demonstrated from the clinical application perspective. The SIFP sensors characterization is performed in the respective electrolyte as well as artificial biofluids, and real-time application of parallel biofluid sampling and sensing is demonstrated on a healthy volunteer followed by a wireless display of SIFP sensors reading on a smartphone. The successful SIFP performance and demonstration of its competence for real-time parallel biofluids sampling and analysis exhibit its potential to revolutionize existing medical analysis with non-invasive point-of-care analysis for precision diagnosis.

Experimental

Fabrication of SIFP's Sensors and Electrodes

The SIFP's sensor array, including electrodes for reference and ion-selective sensor's electrodes and electrodes for anode and cathode of stimulation module, was fabricated on a PET film (125 µm) by a screen printing method. Each electrode corresponding stencils were laser-patterned in a PET film. Reference electrodes and conductive lines were fabricated by printing Ag/AgCl ink, whereas carbon paste was used for printing Cl^- and Ca^{2+} ion-selective sensor's working electrodes, followed by 20 mins curing at 80° C. The polyurethane (PU) layer printed on top of printed electrode layers followed by 1 hr curing at 80° C form the encapsulation layer. Similarly, the anode and cathode stimulation electrode layers were fabricated using Ag/AgCl ink printing (20 mins curing at 80° C)

Lab on a Chip Accepted Manuscript

 This journal is © The Royal Society of Chemistry 20xx

View Article Online
DOI: 10.1039/D2LC00183G

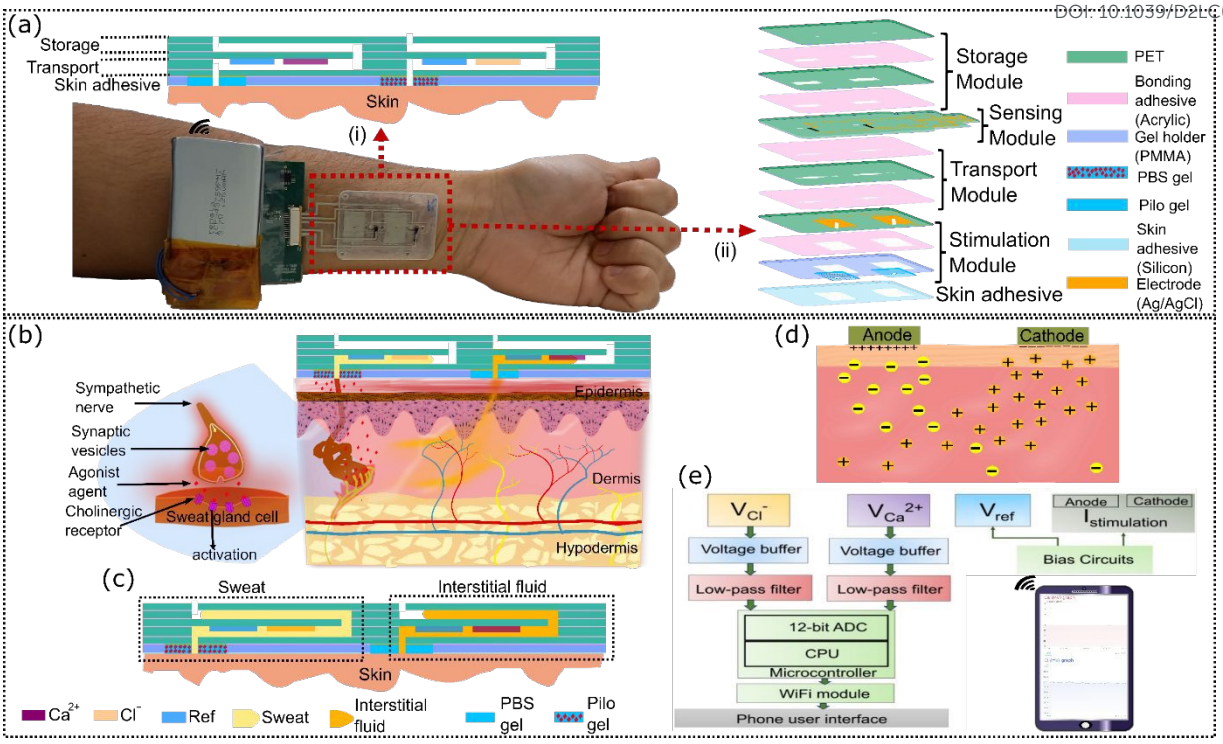


Fig. 1 Overview and working principle of the SIFP. (a) Optical image of SIFP attached to the wrist of the subject, schematic illustration of the cross sectional view of the SIFP (i), exploded view of the SIFP with stimulation, transport, sensing, and storage modules (ii). (b) Schematic illustration of the secretion of sweat and ISF through chemical stimulation reverse iontophoresis. (c) Schematic illustration of sweat and ISF flow through their respective transport module to the storage module of the SIFP fluidics. (d) Schematic representation of the counter-ion attractions, anions are attracted to the anode, and cations are attracted towards the cathode of the electrodes. (e) Block diagram of the PCB used for stimulation and analysis of biofluids and smartphone interface for SIFP communication.

followed by printing the PU encapsulation (1 hr curing at 80° C). Finally, Cl^- and Ca^{2+} ion-selective sensors were fabricated by drop-casting 2 µL of Cl^-, and Ca^{2+} membrane solutions, respectively, onto their respective working electrodes followed by drying in the ambient environment. The fabricated Ag/AgCl reference electrode was coated with reference membrane solution (5 µL). More details related to materials, preparation of membranes, and measurements are provided in Supporting Information.

Fabrication of fluidics modules and SIFP

The optimized transport and storage fluidics modules features were laser engraved on PET substrate. Briefly, the transport fluidics module's fine features such as inlet channel, sensing chamber, and outlet channel with an outlet to the storage module were engraved with a single pass of 40% laser power, a 1% motion stage speed, and 6000 Hz laser pulses. The storage module features were fabricated with parameters of 25% of laser power, 0.8% motion stage speed, and 6000 Hz laser pulses frequency in a single pass. 7% laser power with 0.5% motion stage speed and 1000 Hz laser pulses frequency (single pass) were used for double-sided engraving adhesives (ARcare 92712, Acrylic) and skin adhesives (ARclear 8932EE, Silicone). The stimulation module's gel holder layer was fabricated on a 500 µm PMMA film using the laser pass parameters of 15% laser power, 0.3% pass speed, and a laser pulses frequency of 6000 Hz in a single pass. The SIFP was obtained by vertical integration of the featured stimulation layer, fluidics transport layer, sensing layer, and storage layer in a 3D-direction using patterned adhesives. An Ecoflex adhesive was used to fix the ago tubes (1mm diameter) at the inlets of the ISF and sweat fluidics. The prepared pilogel and PBS gels are poured into the SIFP's respective gel holding voids, then solidified at 4 °C for 1 h. A pattered medical adhesive film was attached to SIFP for mounting patches to subject epidemics.

RESULTS AND DISCUSSION

Design, principle, and interfacing of the SIFP

The operation of the SIFP consists of a simultaneous sampling of ISF and sweat biofluids by iontophoresis and reverse iontophoresis process, the passage of biofluids through their respective pathways, wireless multiplexed monitoring of ISF Ca^{2+} and sweat Cl^- ions, and storage of the bio-fluid in their respective compartments for future analysis. The design consideration of the SIPF patch includes the

Published on 07 March 2022. Downloaded by University College Cork on 3/8/2022 3:24:05 PM.

Lab on a Chip Accepted Manuscript

View Article Online
DOI: 10.1039/D2LC00183G

ARTICLE

Published on 07 March 2022. Downloaded by University College Cork on 3/8/2022 3:24:05 PM.

necessity of the smallest biofluid stimulation region, sufficient biofluid collection for analysis in minimum time, the geometrical strategy of the ion-selective sensors for better signal acquisition, engineering of microfluidics that enables proper implantation of the sensors as well as the efficient biofluid sampling and storage, and optimal inter-facing of the patch to the skin and electronics. The wrist attached SIFP is illustrated in Fig. 1a along with its cross-sectional (Fig. 1ai) and exploded views (Fig. 1aii). As shown in the figure, the SIFP has a vertical integrations of the stimulation, transport, sensing, and storage modules that facilitate biofluids induction, sampling, carriage, analysis, and storing of fluids, respectively, in a single epidermal skin patch. Cost-effectiveness (compared to a patch fabrication utilizing multistep photolithographic process, cleanroom facilities, and long processing time), user-friendliness, strain-free data acquisition, and simplicities in-circuit interfacing are the main factors considered for the material selection and fabrication procedures to realize the SIFP. The engineered implementation of the SIFP sensor arrays facilitates easiness in readout circuit inter-facing. The attachment of the SIFP to the skin is enabled through a medical-grade skin adhesive film that provides tight sealing without skin irritation.

The SIFP stimulation module consists of anode and cathode electrodes printed on a polyethylene terephthalate (PET) substrate coupled with a pilogel and a PBS gel, respectively, through a polymethyl methacrylate (PMMA) gel coupler. The coupled gels act as the interface between electrodes and epidermis, thus preventing skin burning by providing sound isolation. Pilogel is loaded with cholinergic agonists (e.g., pilocarpine) that gets repelled to the epidermis during the iontophoresis process and binds to the sweat gland's acetylcholine receptors to induce sweat (Fig. 1b). The human skin's negative charge and counterions migration cause the parallel electroosmotic flow of the interstitial fluid toward the cathode.[50] Thus, sweat is induced towards the anode, while ISF collected is collected at the cathode compartment (Fig. 1b). As shown in Fig. 1c, electro repulsion causes the attraction of anions at the anode side and cations at the cathode side. The induced biofluids are rapidly transported to their respective fluidics collection compartments through the SIFP's capillary tube inlets without causing the mixing of biofluids.

SIFP's microfluidics combines the biofluids transport and storage module, and they are laser engraved on a PET substrate based on computational optimization. The integration of these modules to the SIFP facilitates prevention of contamination of ion-selective sensor array surface due to direct contact with epidemics, eliminates unstable sensor reading due to evaporation of biofluids, avoids mixing of biofluids by rapid sampling during its excretion starts, and enables storing of fluids for future analysis. The transport module consists of a 1 mm diameter inlet coupled to a stimulation module through the capillary tube, an inlet channel with a width of 150 µm links to a sensing chamber of varying width toward its outlet, and a 2mm diameter outlet connects to a storage module. The engineered and optimized design of the SIFP's transport module enables quick uptake and fast transport of the biofluids by eliminating the backpressure in the flow as its excretion starts. The osmotic pressure and capillary action at the SFIP's inlet allow the flow of the biofluids to the storage module of the SIFP. The storage module is designed with a maximum capacity of 20 µL biofluid. The storage capacity of the biofluids can be in-creased by redesigning this module based on the application of biofluid collection.

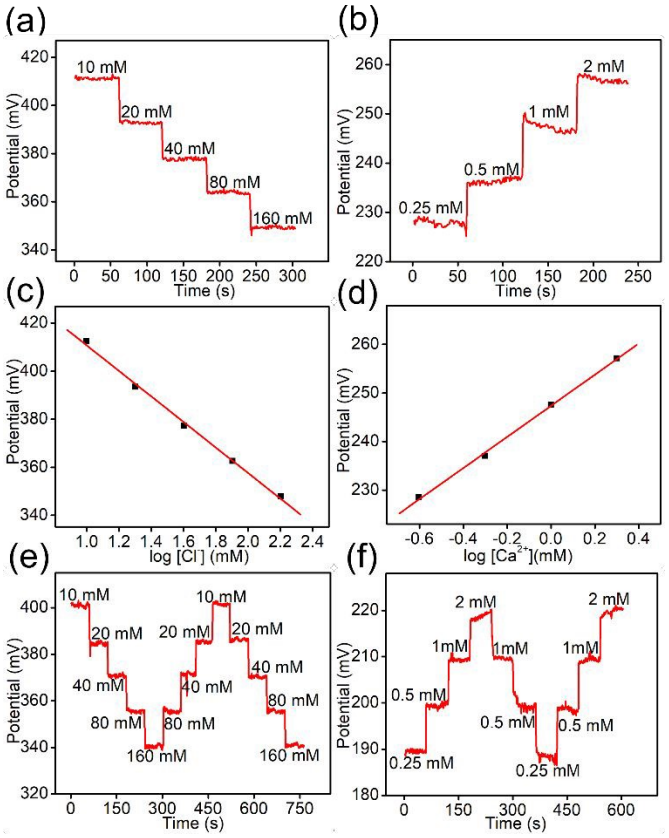


Fig. 2 Response of the SIFP ion-selective sensors in their respective electrolyte. (a) Response of the Cl^- ion-selective sensor to different concentrations of Cl^- ions. (b) Response of the Ca^{2+} ion-selective sensor to different concentration of Ca^{2+} ions. (c) Linear relationship between open circuit potential and Cl- ion concentrations in logarithmic scale. (d) Linear relationship between open circuit potential and Ca^{2+} ions concentrations in logarithmic scale. (e) Repeatability of the Cl^- ion-selective sensor when with cyclic variation of Cl^- ion concentrations from 10 mM to 160 mM. (f) Repeatability of the Ca^{2+} ion-selective sensor when with cyclic variation of Ca^{2+} ion concentrations from 0.25 mM to 2 mM.

Lab on a Chip Accepted Manuscript

View Article Online
DOI: 10.1039/D2LC00183G

Published on 07 March 2022. Downloaded by University College Cork on 3/8/2022 3:24:05 PM.

Finally, the SIFP's sensing module comprises potentiometric sensors developed by a screen printing process on a PET substrate followed by membrane coating and integrated into their respective biofluid compartment (Fabrication details provided in the Experimental section). Carbon-based ink and Ag/AgCl ink are used to fabricate ion-selective electrodes (ISE) and reference electrodes, respectively. Calcium ionophore II (ETH 129) based membrane is used for the selective sensing of the Ca^{2+} from ISF, whereas Cl^- detection from the sweat is achieved by tridodecylmethylammonium chloride-based membrane. The chloride saturated polyvinyl butyral (PVB) membrane coating on Ag/AgCl reference electrode provides stable potential at different ionic strengths avoids the voltage drift by preventing the interaction of Cl^- ions with reference. The intelligent design of the sensor's conductive path enables easy interfacing with the printed circuit board (PCB). As shown in Fig. 1e, PCB design includes separate voltage buffers and filters for Ca^{2+} and Cl^- ISE's signal acquisition and conditioning, the reference bias circuit, and the microcontroller unit (MCU) interfacing for data processing and transfer. The MCU includes a 12 bit analog to digital converter (ADC), which converts incoming analog data to the digital signal, and the processed data is wirelessly transmitted to the host device using an on-chip WIFI unit. An iontophoretic unit, which includes a booster with a current converter for setting a stimulation current and a switch for controlling the duration of iontophoresis is coupled to the main part of the PCB. The switch enables the selection of the stimulation module and sensing module. An android based application developed on a smartphone facilitates instantaneous graphical visualization of the real-time SIFP data, whereas the incorporated cloud storing facility helps retrieve the recorded data for further analysis. The SFIP is powered by the lithium-ion polymer rechargeable cell.

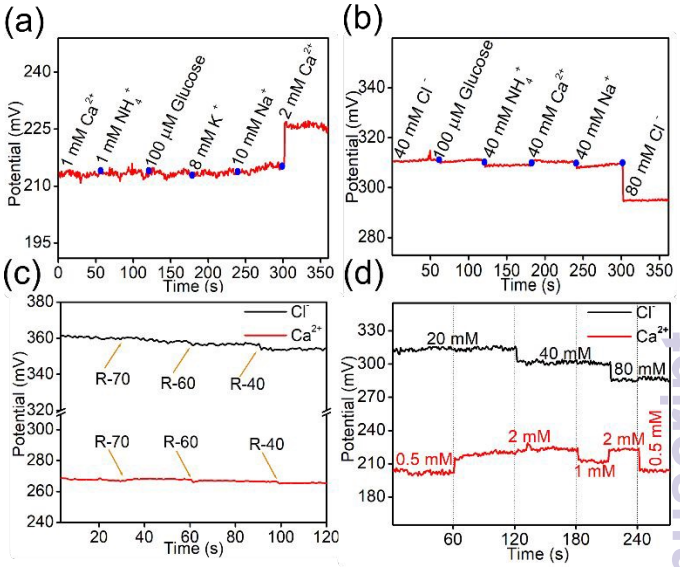


Fig. 3 Characterization of the SIFP ion-selective sensors. Selectivity study of the (a) Ca^{2+} and (b) Cl^- ion-selective sensor in the presence of the physiologically relevant probable interfering ions. (c) Response of the Ca^{2+} and Cl^- ion-selective sensors during 70mm, 60mm, and 40mm bending states. (d) Combined in-vitro operation of the Ca^{2+} and Cl^- ion-selective sensors.

Characterization of SIFP sensors

The SIFP's chloride and calcium ion sensors performance was evaluated in their corresponding electrolyte solution with physiologically pertinent concentrations of Cl^- and Ca^{2+} ions present in sweat and ISF. Fig. 2a shows the response of the Cl^- ion sensor in chloride electrolyte with varying 10-160 mM Cl^- ion concentration. Similarly, the Ca^{2+} ion sensors' response in calcium electrolyte with varying concentrations of 0.25-2 mM Ca^{2+} ion is shown in Fig. 2b. Both Cl^- ion sensor and Ca^{2+} ion sensor exhibited near-Nernstian response with sensitivities 53.1 mV/decade and 32.0 mV/decade, respectively (Fig. 2c,d). The reversibility of the sensors was assessed by recording their responses to sequential changes of respective ion's electrolyte concentrations in a cyclic manner (Fig. 2e,f). The Cl^- ion sensor showed a mean sensitivity of 52.3 mV/decade with 0.4% relative standard deviation (RSD), whereas the Ca^{2+} ion sensor exhibited a mean sensitivity of 32.9 with 1.1% RSD in one and a half step cycle repetitive measurements. The fast response with very negligible signal differences between cyclic concentration changes of electrolyte indicates the good reversibility and repeatability of the fabricated sensor.

The reproducibility of the sensors was evaluated by recording six fabricated Ca^{2+} ion and Cl^- ion sensors responses in their corresponding electrolyte solutions with varying 0.25- 2 mM Ca^{2+} and 10-160 mM Cl^- concentrations, respectively (Fig. S1a,b). Both Ca^{2+} ion and Cl^- ion sensors showed good reproducibility with a mean sensitivity of 33.1 mV/decade (1.9% RSD) and 52.8 mV/decade (1.5% RSD), respectively. The discrepancies between the absolute potential values of the sensors when exposed to the same analyte concentration, which arises due to the manual drop-casting of membranes, can be corrected by a two-point calibration and setting the baseline value to zero.[36] Fig. 3a,b shows the response of the Ca^{2+} ion and Cl^- ion sensors towards possible physiologically relevant interfering ions present in respective biofluids. The significantly smaller change in the response of the sensors to the added interference ions than the response of the respective targeted ion implies the specificity of the fabricated sensors. Besides that, the fabricated sensors exhibited a good selectivity coefficient over various interfering ions (Table S1). Also, both ion-sensors showed negligible response to the agonist agents used to stimulate biofluids (Fig. S2). In addition, both Ca^{2+} ion and Cl^- ion sensors showed no significant response to their respective biofluids' physically relevant variation of pH or temperature (Fig. S3 and S4).

The stability of sensors was assessed in terms of long-term operation as well as storage duration. As shown in Fig. S5a and b, the Ca^{2+} ion sensor exhibited a potential drop of 1.5 mV/hr, whereas Cl^- ion sensor showed a potential drop of 1.3mV/hr. This study implies the ability of the SIFP sensors for continuous signal acquisition. Fig. S5c and Fig. d show the storage stability of the Ca^{2+} ion sensor and Cl^- ion sensor, respectively. The Ca^{2+} ion sensor showed good

Lab on a Chip Accepted Manuscript

View Article Online
DOI: 10.1039/D2LC00183G

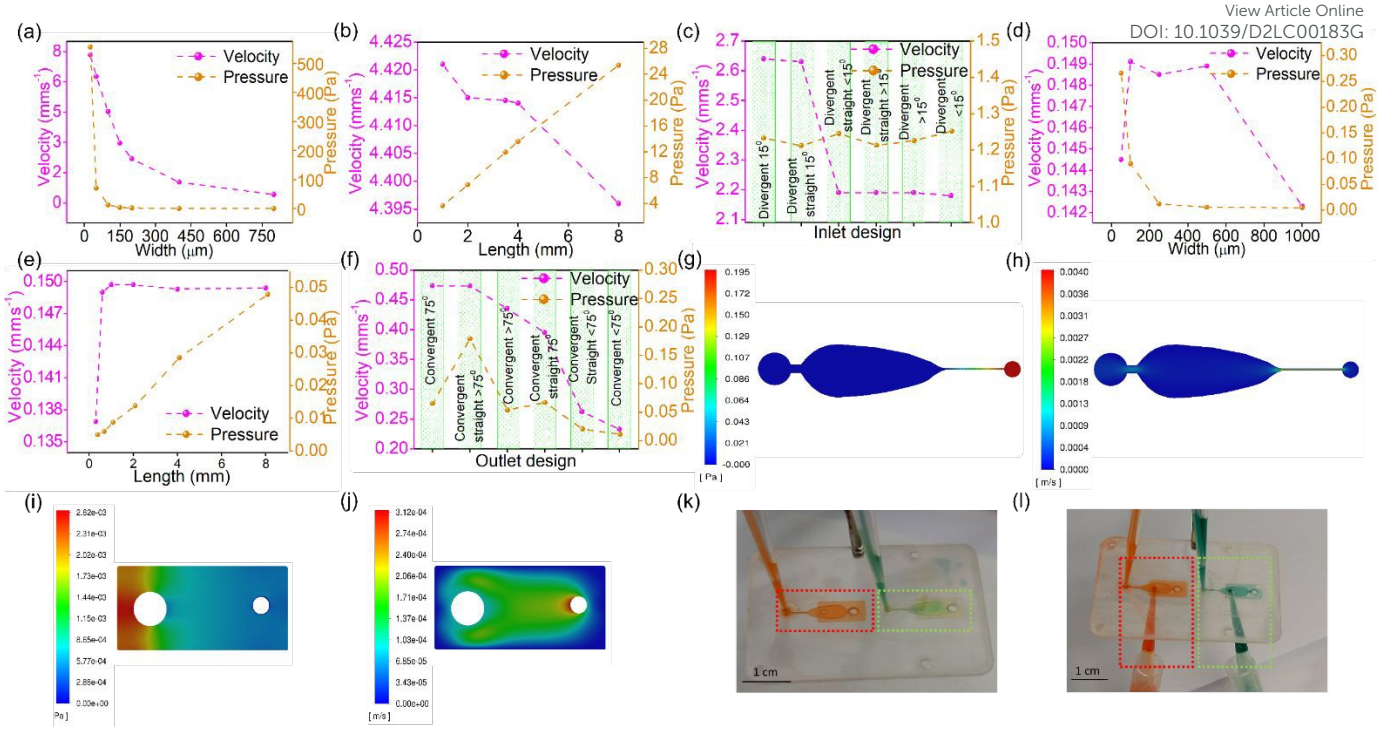


Fig. 4 Optimization, design, and characterization of the SIFP fluidics. The geometries of the transport and storage modules of the SIFP were determined based on computational analysis and Young-Laplace model to obtain maximum fluid flow velocity without backpressure. Velocity and pressure dependence optimization on (a) width and (b) length of the inlet channel. (c) Selection of inlet channel design towards the sensing chamber. Velocity and pressure dependence optimization on (d) width and (e) length of the outlet channel. (f) Selection of outlet channel design from the sensing chamber. SIFP transport module's (g) pressure, (h) velocity counterplots. SIFP storage module's (i) pressure, and (j) velocity counterplots. Optical images of SIFP fluidics leakage test (k) simultaneous flow through ISF and sweat compartment, (l) concept of the continuous simultaneous sampling and withdrawal of biofluids (red indicated region represents ISF flow section whereas, green indicated region represents sweat flow section).

stability in sensitivity up to three weeks, and relative sensitivity was reduced to 84.41% after four weeks. However, the Cl^- ion sensor exhibited non-negligible sensitivity changes from the third-week beginning and found be 79.78% on the fourth week. The proper calibration in advance of the experiments enables the usage of the SFIP sensors even after a specific storage duration. The mechanical stability of fabricated sensors was evaluated by bending the sensors a different angles (Fig. S6 and S7) as well as recording the sensing response of the sensors before and after applying different bending angles (Fig. 3c). The small change in resistance and good sensing signal stability during different angles deformation shows the suitability of the fabricated sensors for wearable applications. The cross-talk interference between the Cl^- ion and Ca^{2+} ion sensors was estimated by recording the combined response of the sensors with successive variations of each sensor's respective target analyte concentrations (Fig. 3d). The good signal response of each sensor to their target ions irrespective of the counter ion sensor's variation of concentration indicates the reliability of the SIFP sensors for simultaneous biofluids monitoring.

Design, integration, and characterization of SIFP fluidics

The fluidics design for the SIFP was optimized based on computational fluid dynamics using ANSYS FLUENT 2021 R1 academic and Young-Laplace model.[58] The fluidics transport module features such as the inlet channel, the outlet channel, and shape of the inlet to the sensing chamber and from the sensing chamber to the outlet were optimized to obtain the maximum fluid flow velocity to ensure adequate biofluid sampling for analysis. The height of the fluidic structure was kept as a fixed constraint, which is the total thickness of the PET and the adhesive layers used for the fluidics fabrication. The storage module was designed to provide a constant flow rate without causing back pressure and dead volume. The geometries (length and width) of the inlet and outlet channels of the transport and storage modules of the SIFP were selected based on the pressure and the velocity counterplots analysis to obtain the maximum fluid flow velocity without backpressure. Then, the geometry of the inlet joint (with converging angle) to the sensing chamber and the geometry of the sensing chamber joined to the outlet (with convergent angle) were determined based on the Young-Laplace model and pressure and velocity counterplots analysis to have the maximum fluid flow velocity. The geometry of the sensing chamber was selected to get a feasible connection to the optimized inlet and outlet geometries and an appropriate placement of the ion-selective sensors without hindrance to the flow. Both sweat and ISF fluidics modules of SIFP were designed with the same geometries, facilitating the comparison of both compartment's fluids flow rates at different physiological conditions. As shown in Fig. 4a, the fluid's pressure and the velocity profile decrease with the increase in the channel's width (after 150 µm). Similarly, the flow velocity profiles drop drastically with the increase of channel length (after 4.5mm) (Fig. 4b). Thus, 150 µm and 4.5mm was selected as a SIFP fluidics inlet channel width and length, respectively, for the transport module.

Published on 07 March 2022. Downloaded by University College Cork on 3/8/2022 3:24:05 PM.

Lab on a Chip Accepted Manuscript

This journal is © The Royal Society of Chemistry 20xx

View Article Online
DOI: 10.1039/D2LC00183G

Published on 07 March 2022. Downloaded by University College Cork on 3/8/2022 3:24:05 PM.

The inlet shape towards the sensing chamber and the outlet shape from the sensing chamber were evaluated based on pressure and velocity profiles with different shapes and angles of the joints (Fig. S8). The channel inlet divergent joint to sensing chamber with angle β=15° and a convergent outlet joint from the chamber with angle β'=75° were selected as optimum design parameters, which provides the maximum fluid flow velocity (Fig. 4c,f). The design of the sensing chamber with a varying width from inlet to outlet facilitates proper integration of the ion-selective sensors without any obstruction to the flow by avoiding any dead volume inside the chamber. A channel width of 500 µm was selected for the outlet channel since a drastically decreasing velocity profile was observed after that (Fig. 4d). The outlet channel velocity profile exhibited an increasing trend with the channel length, and it appeared as an almost constant profile at 600 µm length, whereas the pressure profile showed a linear variation with length (Fig. 4e). Thus, a channel length of 600 µm was selected for the outlet. A diameter of 2mm was chosen for the inlet to the storage module of the SIFP, to enable fast passage through the transport module without any backpressure. The storage module was fabricated to allow an accumulation of 20 µL of biofluid, and the optimized design facilitates a constant flow towards the outlet of the respective biofluids' storage modules. In addition, a 1mm diameter outlet of the SIFP at the end of the storage module ensures the withdrawal of the collected biofluid after its complete filling.

Fig. 4g and Fig. 4h depict the pressure distribution and velocity counterplots, respectively, for the transport module of the SIFP. The maximum pressure at the fluid inlet of the channel was observed and maintained a constant pressure towards the outlet of the transport module. Similarly, after a fast flow of the fluid through the inlet channel, the continuous fluid velocity profile was maintained inside the sensing chamber of the transport module of the SIFP, which enables stable readings from the ion-selective sensors. The velocity counter-line plots reveal that the fluid meniscus advances radially to the inlet of the sensing chamber (Fig. S9a). The pressure distribution plots of the storage module show that the maximum pressure was experienced at the inlet through which the fluid enters from the transport module, and then it maintains a constant pressure towards the outlet (Fig. 4i). The velocity distribution was almost stable through the module's center towards the outlet, which was evident from the velocity path-line distribution (Fig. 4j and Fig S9b). A schematic illustration of the SIFP fluidics fabrication is shown in Fig. S10. A series of tests were performed to assess the fabricated microfluidics efficiency for maintaining a leakage-free fluid flow by using the flow of a colored dye with a maximum flow rate of 5µL/sec maintained using a pump. Fig. S11a and Fig. S11b show an optical image of the fluid flow through the transport module of the ISF compartment and the filling the storage compartment, respectively. Similarly, the fluid flow through the sweat compartment is shown in Fig. S11c and Fig. 11d. Simultaneous flow through both compartments is depicted in Fig. 4k, whereas the concept of the continuous simultaneous sampling of biofluids and withdrawal is shown in Fig. 4l. The leakage-free incessant simultaneous flow of fluid even at a higher flow rate reveals the reliability of fabricated SIFP microfluidics module for simultaneous sampling, carriage, and storage of the biofluids.

The characterization of the sensor array with the integrated fluidics was performed by recording the responses of the ion-selective sensors while maintaining a constant flow of the artificial biofluids in the respective compartment. Fig. 5a and Fig. 5b depict

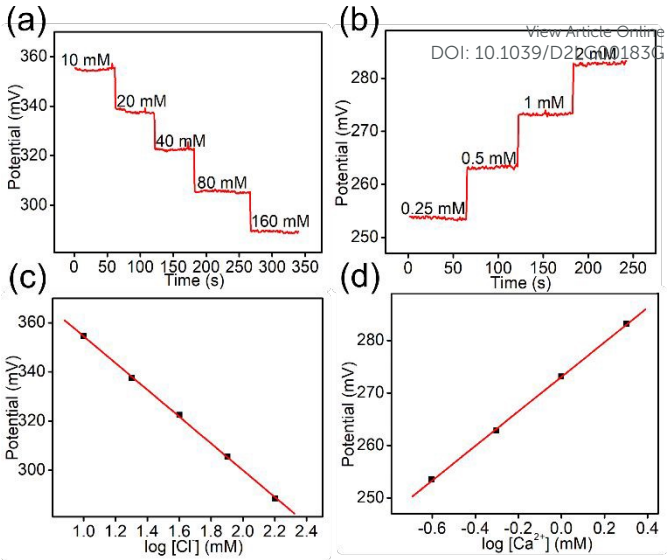


Fig. 5 Response of the SIFP ion-selective sensors in artificial biofluids. (a) Response of the Cl^- ion-selective sensor to different concentrations of Cl^- ions in artificial sweat. (b) Response of the Ca^{2+} ion-selective sensor to different concentrations of Ca^{2+} ions in artificial ISF. (c) The linear relationship between open circuit potential and artificial sweat Cl^- ion concentrations in logarithmic scale. (d) The linear relationship between open circuit potential and artificial ISF Ca^{2+} ions concentrations in logarithmic scale.

the Ca^{2+} ion sensor and Cl^- ion sensor response, respectively, and their corresponding calibration plots are shown in Fig. 5c and Fig. 5d. Both Ca^{2+} ion Cl^- ion sensors exhibited a near-Nernstian response with the sensitivity of 32.9 mV/decade and 54.2 mV/decade, respectively, which reveals the capability of the SIFP sensors for complex biofluid analysis. To further evaluate the stability of the sensor's responses during the epidermal interfaces, the PCB interfaced SIFP system filled with the respective electrolytes in each sensor's biofluid compartment was fixed to the subject wrist, and the sensors' responses were recorded while the subject was undertaking various daily routines as well as different arm gestures (Fig. S12 and Fig. S13). The stable sensors responses with negligible signal fluctuations during these activities show the robustness of the fabricated SIFP for biofluid analysis with minimal body movement. However, the main application of the fabricated SIFP lies in biofluids monitoring on sedentary condition individuals.

Sweat and ISF sampling characterization

The amount of the biofluids secretion depends on the appropriate selection of gel, applied current intensity, and duration of the stimulants delivered to activate the glands. The coupling of the pilogel to the anode and PBS gel to the cathode was chosen since it shows the best results for an adequate fluid flow through the channel for the analysis (Table S2). After the coupling of the respective gel, the simultaneous analysis of the biofluids' flow through the channel was performed. The stimulation parameters were optimized by applying different current intensities for a different duration. Even though the application of the higher stimulation current intensities induced higher biofluid quantities, to minimize skin irritation, the stimulation current intensity was limited to 1.3 mA, which also ensured sufficient biofluid sampling for analysis. Similarly, the stimulation duration was optimized to 10 min, which enabled the

Lab on a Chip Accepted Manuscript

View Article Online
DOI: 10.1039/D2LC00183G

ARTICLE

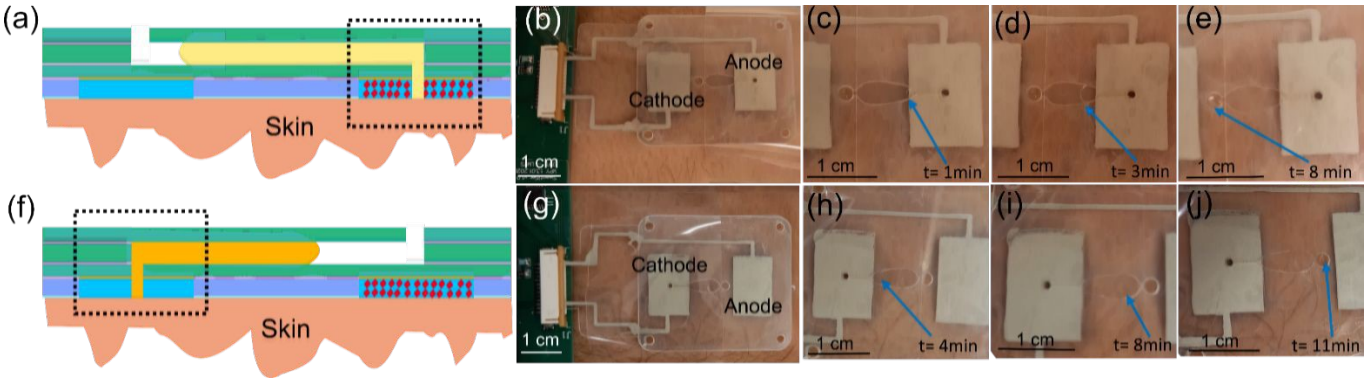


Fig. 6 Characterization of sweat and ISF secretion. (a) Schematic illustration of the sweat secretion and sweat flow in the transport module through the inlet of the anode compartment. The stimulation module was activated for 10 min for the iontophoretic delivery of pilocarpine, which activates the sweat gland for sweat induction at anode compartment. (b) For the individual sweat flow analysis, the transport module was integrated into the anode compartment of the stimulation module and attached to the subject's wrist. (c-d) Optical images of the flow dynamics of the secreted sweat through the sweat transport module after sweat flow initiation (advancing fronts of the fluids at various times is indicated). (e) The sweat flow reached the outlet of the transport module in 8 min. (f) Schematic illustration of the ISF extraction and ISF flow in the transport module through the inlet of the cathode compartment. The reverse iontophoresis process was performed by activating the stimulation module for 10 min, which causes electro-osmotic flow and extraction of ISF at the cathode compartment. (g) For the individual ISF flow analysis, transport module was integrated into the cathode compartment of the stimulation module and attached to the subject's wrist. (h-i) Optical images of the flow dynamics of the secreted ISF through the transport module after ISF flow initiation (advancing fronts of the fluids at various times is indicated). (j) The ISF flow reached the outlet of the transport module in 11 min.

higher ISF and sweat flow with adequate sampling for analysis compared to the lower stimulation period (Fig. S14). It was also observed that a duration longer than 10 min causes skin irritation.

To further analyze the efficiency of the biofluid flow through their respective transport modules of the SIFP, sweat and ISF flow were monitored individually by integrating the corresponding transport module (sweat/ISF) to the respective stimulation module compartment (anode/cathode) and performing stimulation at the optimized parameters (Fig. 6a,f). For the sweat flow analysis, the transport module (without sensing and storage modules) was integrated into the anode compartment of the stimulation module and firmly attached to the subject's wrist with PCB interfacing, as shown in Fig. 6b. The sweat induction process was executed by activating the stimulation module for 10 min to induce the sweat gland due to iontophoretic delivery of pilocarpine, which causes sweat secretion. The secreted sweat slowly accumulated the transport module through the inlet at the anode compartment. The time taken by sweat flow to reach the outlet of the transport module was monitored for estimating sweat flow rate. Fig. 6c-e shows the optical images of flow dynamics of the sweat. It was observed that the sweat flow advances to the sensing chamber after 1 min of the sweat flow initiation, and the flow reached the outlet in 8 min. Thus, the sweat flow rate was calculated to be 1.25 µL/min based on the volume of the transport module and the time taken by the sweat flow to reach the outlet. The 1 cm^2 stimulation area enabled the sweat flow into the fluidics, and the sweat rate per gland was estimated to be 8.3 nL/min. Similarly, to analyze the ISF flow, the transport module (without sensing and storage modules) was integrated into the cathode compartment of the stimulation module and tightly attached to the subject's wrist with PCB interfacing, as shown in Fig. 6g. The reverse iontophoresis process was conducted by activating the stimulation module for 10 min, which causes electro-osmotic flow and extraction of ISF at the cathode compartment. The extracted ISF was slowly drifted to the transport module through the inlet at the cathode compartment. The ISF flow rate was assessed based on the time taken by ISF flow to reach the outlet of the transport module. Fig. 6h-j shows the flow dynamics of the ISF through the transport module. Slower flow dynamics were observed for ISF than for sweat, and ISF reached the outlet of the patch in 11 min with a flow rate of 0.91 µL/min. These characterization results indicate the efficiency of the fabricated patch for biofluids secretion and carriage with the optimized parameters of the stimulation process.

On-body biofluids analysis using SIFP

The Simultaneous sampling of the different biofluids from the vascular space and study of the relationship between these biofluids as well as various markers present in them at various physiological conditions are intrinsically significant to analyze the behavior of the different body fluids compartments and their electrolyte balance at

Published on 07 March 2022. Downloaded by University College Cork on 3/8/2022 3:24:05 PM.

Lab on a Chip Accepted Manuscript

View Article Online
DOI: 10.1039/D2LC00183G

ARTICLE

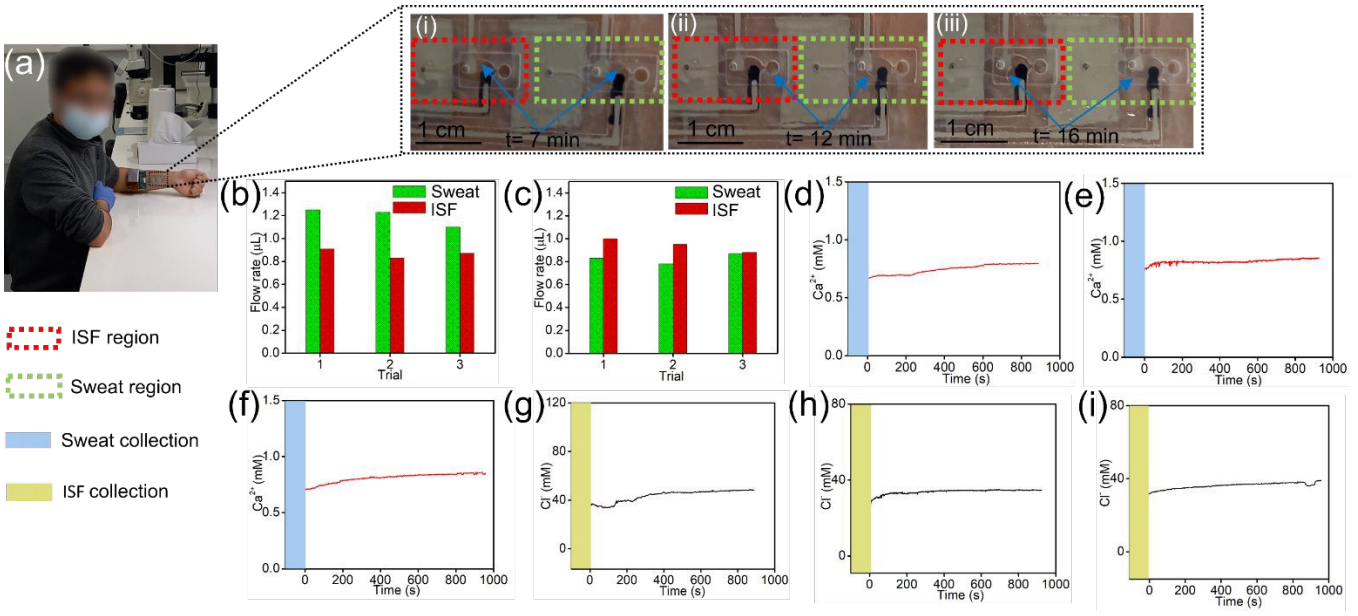


Fig. 7 On-body biofluid analysis. (a) The SIFP is attached to the subject wrist for biofluid secretion, collection, storage, and the sensors data are transmitted to the smartphone-based application and cloud for analysis, (i-iii) optical images of the flow dynamics of the secreted ISF and sweat through the respective ISF (red indicated region) and sweat (green indicated region) transport and storage modules of the SIFP (advancing fronts of the fluids at various times is indicated). Sweat and ISF flow rate (b) during hydration (c) dehydration conditions. (d-f) ISF's Ca^{2+} ion and (g-i) sweat's Cl- ion concentration profiles of the subject during (d, g) morning, (e, h) afternoon, and (f, i) evening analysis.

the different body's physiological states. This analysis could potentially provide emergent information on the critical conditions of the body when undergoing different situations, and It might lead to predicting several medical and physiological health statuses. However, there has been no sufficient analysis due to limitations in the technology to simultaneously access and sample the different body fluids. The SIFP presented here facilitates simultaneous sampling, transport, and storage of ISF and sweat and analysis of ions present in them. As an initial effort, SIFP capability to monitor the relationship between ISF and sweat flow-rate and the efficiency of monitoring sweat Cl- and ISF Ca2+ concentrations as a model system at different physiological conditions such as hydration and dehydration states of the body was demonstrated on a healthy volunteer. The Sweat and ISF flow rates were estimated by analyzing the time taken by the respective sweat and ISF flow to reach the outlet of the corresponding SIFP transport module, whereas Ca2+ ion and Cl- ion-concentration was estimated by recording stabilized responses from ion-selective sensors after filling the respective ISF and sweat compartment of the storage module and further stopping of the fluids flow occurs. A two-point calibration method was executed before as well as after each trial for calibrating the SIFP sensors. Ion-selective sensors based on tridodecylmethylammonium chloride membrane for Cl^- sensing and ETH129 membrane for Ca^{2+} sensing were already demonstrated the well-established validation with the ion-chromatographic measurements, which enables the development of ion-selective sensors for real sample analysis based on these membranes[49,59]. The SIFP also validates this by showing a consistent relationship between one of its sensor's concentration profiles with ion-chromatographic measurements, which reveals the reliability of the SIFP for biofluid analysis (Fig. S15). To perform the on-body biofluid analysis, the PCB interfaced SIFP was well fixed to the wrist of the healthy volunteer, as shown in Fig. 7a. The stimulation process was executed with a 10 min duration by activating the stimulation module of the SIFP. The iontophoresis and reverse iontophoresis process initiates the secretion of sweat and ISF, which slowly transport the fluids through the corresponding biofluids transport modules and accumulates them to the respective storage modules. The SIFP sensor module was triggered after both biofluids' flow was saturated and they filled the storage module by its maximum quantity, which enables to acquire stable readings from the sensor array for accurate measurements of the biofluids' ionic profiles. The SIFP readings were displayed on the

Published on 07 March 2022. Downloaded by University College Cork on 3/8/2022 3:24:05 PM.

Lab on a Chip Accepted Manuscript

View Article Online
DOI: 10.1039/D2LC00183G

ARTICLE

Published on 07 March 2022. Downloaded by University College Cork on 3/8/2022 3:24:05 PM.

smartphone interfaced application by wireless transmission and also facilitated storing in the could platform for future retrieval for analysis.

Fig. 7a(i)-(iii) shows the simultaneous sampling and transport of the ISF and sweat in SIFP with different time intervals. From the optical image of the flow in the ISF compartment, it was observed that ISF crossed half portion of the transport module in 7 minutes and reached the outlet of the transport module in 12 minutes with a flow rate of 0.83 µL/min. The ISF flow arrived near to outlet of the storage module in 16 minutes, and the flow was found to be saturated after that. The sweat flow covered 90% of the transport module in 7 minutes and arrived at the outlet of the storage module in 16 min. The sweat flow rate was approximately 1.25 µL/min, and this flow was recorded in a hydrated volunteer. The three trial experiments conducted during hydrated conditions exhibited a similar trend of elevated sweat flow rate than ISF (Fig. 7b). A more precise flow rate can be estimated by interfacing with flowrate modules and admittance-based measurements. In contrast, the sweat flow rate was observed to be very slow compared to ISF flow during dehydration states, as shown in Fig. S16. In this case, sweat reached the outlet of the transport module in 12 minutes, and the estimated flow rate was 0.83 µL/min. The ISF flow was found to stop at 15 min by accumulating half of the storage module, whereas sweat flow was stopped without even covering the half portion of the storage module. A similar trend of higher ISF than sweat flow was observed in two trial experiments on a healthy volunteer with a dehydrated state, whereas one trial showed almost the same flow for both ISF and sweat (Fig. 7c). The phenomena of observation of less sweat flow rate than ISF flow during dehydration can be explained based on the physiological fluid balance on the body, which is the combination of intracellular and extracellular (interstitial and intravascular space) fluid. Dehydration causes a reduction in the intravascular fluid. However, Nose et al. reported that the decrease in the extracellular fluid amount is much smaller than the sweat loss.[60] In addition, extracellular fluid is balanced by drawing the fluid from the intracellular space if any reduction in fluid occurs. The decrease in the sweat rate after dehydration was also reported in Fortney et al.'s studies.[61] However, establishing a consistent relationship between ISF and sweat flow rate and their dependency on hydration and dehydration required large population studies, which is beyond the scope of this study. Fig. 7d-i shows the SIFP's ion-sensors readings recorded from the on-body application on a healthy volunteer during different day periods. The stabilized response from Ca^{2+} ion and Cl^- ion sensors after filling the respective biofluid's storage module and further stopping the fluids flow were considered to estimate the ion-concentration level. Ca^{2+} ion sensor responses from the ISF compartment did not show much deviation during different periods and reflected a concentration profile of less than 1 mM. However, Cl^- ion sensor reading reflected a concentration profile of above 40 mM during the morning compared to the afternoon and evening measurements, during which the Cl^- ion sensor recorded a concentration profile of less than 40 mM. This reduction in concentration profiles may be related to the diet and dehydration states [62]; however, the exact interpretation of these observations is beyond the current focus of the study. This on-body analysis affirms the capability of the SIFP for simultaneous analysis of ISF and sweat, including different phycological states of individuals and providing corresponding concentration profiles of the ions in biofluids. This proof-of-concept experiment can further be extended to the investigations on large populations, which might bring the potential application of SIFP in personalized healthcare monitoring and predicting individuals' physiological statuses.

Conclusions

The Simultaneous analysis of biofluid and insight information of the biomarkers will revolutionize the medical field in terms of precision diagnosis and medication. The present work demonstrated such an effort by realizing the wearable biofluids patch, SIFP, for simultaneous secretion, sampling, storing the ISF and sweat, and detection of the respective counter ion. The clean-room free cost-effective fabrication of SIFP includes the development of the sensors by printing and coating ion-selective membranes and coupling with laser engraved microfluidics features and a biofluids stimulation system, which enables simultaneous excretion of biofluids. The developed SIFP's Cl^- and Ca^{2+} ion-selective sensors exhibited good sensitivity, reproducibility, repeatability, and acceptable stability for use in real biofluid monitoring. The judicial design and interfacing of microfluidics facilitated intelligent transport and analysis by storing biofluids and eliminating sensor contamination by direct skin contact, evaporation of the secreted biofluids, and mixing of biofluids. The electronic interfacing and wireless data transmission of the SIFP demonstrate its standalone operation capability for simultaneous decoding of biofluids and biomarker profiles without the requirement of separate external hardware. The proof of concept study on a health volunteer by demonstrating the analysis of the dynamics of biofluids for hydration and dehydration states and profiling of the concentrations of ion's in different periods of the day reveals the SIFPs ability for real sample analysis and predicting the different conditions of the body for personalized healthcare use. The future work includes the miniaturization of the system, extensive population studies for generating large datasets, integration of multiple bio-

Lab on a Chip Accepted Manuscript

View Article Online
DOI: 10.1039/D2LC00183G

marker sensors, analysis of biofluids from different body locations, and its correlation with blood analytes to lead to a smart non-invasive point of the care system for personalized diagnostics. We envisage that the manifestation of the simplified SIFP fabrication process and its capability of real sample analysis could bring a breakthrough impact in precision diagnosis by simultaneous monitoring of multiple biofluids.

Conflicts of interest

The authors declare no conflicts of interests.

Acknowledgements

Acknowledgments to the SNF SINERGIA project grant number CRSII5_177255, Prof. Herbert Shea, head of the Soft Transducers Lab (LMTS), EPFL for laboratory resources, implementation of idea with the concept of biofluid storage, and valuable time for discussions. Dr.Danick Briand, EnviroMEMS lead for resources and valuable time for discussions, Dr. Mathieu Saubade and Dr. Céline Lafaye, division of physical medicine and rehabilitation, Centre hospitalier universitaire vaudois (CHUV), Lausanne, for sweat samples and ion-chromatographic measurements, Valentin Py, LMTS, EPFL, for his help with developing the SMT-based PCB, and Dr. Peter Van der Wal, EPFL, for resources, valuable time for discussions, and helping with his strong knowledge and experience in ion-selective devices and electrochemistry during various stages.

References

1 D.-H. Kim, N. Lu, R. Ghaffari, Y.-S. Kim, S. P. Lee, L. Xu, J. Wu, R.-H. Kim, J. Song and Z. Liu, Nat. Mater., 2011, 10, 316–323.
2 S. S. Kwak, S. Yoo, R. Avila, H. U. Chung, H. Jeong, C. Liu, J. L. Vogl, J. Kim, H. Yoon and Y. Park, Adv. Mater., 2021, 2103974.
3 C. Liu, J. Kim, S. S. Kwak, A. Hourlier-Fargette, R. Avila, J. Vogl, A. Tzavelis, H. U. Chung, J. Y. Lee and D. H. Kim, Adv. Healthc. Mater., 2021, 2100383.
4 Y. Lin, M. Bariya and A. Javey, Adv. Funct. Mater., 2020, 2008087.
5 H. Lukas, C. Xu, Y. Yu and W. Gao, ACS Nano, 2020, 14, 16180–16193.
6 Y. H. Jung, J. Kim and J. A. Rogers, Adv. Funct. Mater., 2021, 31, 2008805.
7 R. Hinchet and H. Shea, Adv. Mater. Technol., 2020, 5, 1900895.
8 E. Leroy, R. Hinchet and H. Shea, Adv. Mater., 2020, 32, 2002564.
9 J. R. Sempionatto, I. Jeerapan, S. Krishnan and J. Wang, Anal. Chem., 2019, 92, 378–396.
10 X. He, S. Yang, Q. Pei, Y. Song, C. Liu, T. Xu and X. Zhang, ACS Sens., 2020, 5, 1548–1554.
11 Y. Song, J. Min, Y. Yu, H. Wang, Y. Yang, H. Zhang and W. Gao, Sci. Adv., 2020, 6, eaay9842.
12 J. R. Sempionatto, A. A. Khorshed, A. Ahmed, A. N. De Loyola e Silva, A. Barfidokht, L. Yin, K. Y. Goud, M. A. Mohamed, E. Bailey and J. May, ACS Sens., 2020, 5, 1804–1813.
13 K. Kwon, J. U. Kim, Y. Deng, S. R. Krishnan, J. Choi, H. Jang, K. Lee, C.-J. Su, I. Yoo and Y. Wu, Nat. Electron., 2021, 4, 302–312.
14 J. Zhao, H. Y. Y. Nyein, L. Hou, Y. Lin, M. Bariya, C. H. Ahn, W. Ji, Z. Fan and A. Javey, Adv. Mater., 2021, 33, 2006444.
15 E. Garcia-Cordero, F. Bellando, J. Zhang, F. Wildhaber, J. Longo, H. Guérin and A. M. Ionescu, ACS Nano, 2018, 12, 12646–12656.
16 S. Demuru, B. P. Kunnel and D. Briand, Adv. Mater. Technol., 2020, 5, 2000328.
17 S. Demuru, B. P. Kunnel and D. Briand, Biosens. Bioelectron. X, 2021, 7, 100065.
18 J. Min, J. R. Sempionatto, H. Teymourian, J. Wang and W. Gao, Biosens. Bioelectron., 2021, 172, 112750.
19 S. Emaminejad, W. Gao, E. Wu, Z. A. Davies, H. Y. Y. Nyein, S. Challa, S. P. Ryan, H. M. Fahad, K. Chen and Z. Shahpar, Proc. Natl. Acad. Sci., 2017, 114, 4625–4630.
20 S. Hozumi, S. Honda, T. Arie, S. Akita and K. Takei, ACS Sens., 2021, 6, 1918–1924.
21 J. R. Sempionatto, V. R.-V. Montiel, E. Vargas, H. Teymourian and J. Wang, ACS Sens., 2021, 6, 1745-1760.
22 X. Xuan, C. Pérez-Ràfols, C. Chen, M. Cuartero and G. A. Crespo, ACS Sens., 2021, 6, 2763–2771.
23 J. R. Sempionatto, J.-M. Moon and J. Wang, ACS Sens., 2021, 6, 1875–1883.
24 H. Y. Y. Nyein, M. Bariya, L. Kivimäki, S. Uusitalo, T. S. Liaw, E. Jansson, C. H. Ahn, J. A. Hangasky, J. Zhao and Y. Lin, Sci. Adv., 2019, 5, eaaw9906.
25 Y. Zhao, B. Wang, H. Hojaiji, Z. Wang, S. Lin, C. Yeung, H. Lin, P. Nguyen, K. Chiu and K. Salahi, Sci. Adv., 2020, 6, eaaz0007.
26 A. Bandodkar, S. Lee, I. Huang, W. Li, S. Wang, C.-J. Su, W. Jeang, T. Hang, S. Mehta and N. Nyberg, Nat. Electron., 2020, 3, 554–562.
27 J. Kim, I. Jeerapan, S. Imani, T. N. Cho, A. Bandodkar, S. Cinti, P. P. Mercier and J. Wang, Acs Sens., 2016, 1, 1011–1019.
28 G. Xu, C. Cheng, Z. Liu, W. Yuan, X. Wu, Y. Lu, S. S. Low, J. Liu, L. Zhu and D. Ji, Adv. Mater. Technol., 2019, 4, 1800658.
29 A. Wiorek, M. Parrilla, M. Cuartero and G. A. Crespo, Anal. Chem., 2020, 92, 10153–10161.
30 R. Ghaffari, J. Choi, M. S. Raj, S. Chen, S. P. Lee, J. T. Reeder, A. J. Aranyosi, A. Leech, W. Li and S. Schon, Adv. Funct. Mater., 2020, 30, 1907269.
31 M. Bariya, Z. Shahpar, H. Park, J. Sun, Y. Jung, W. Gao, H. Y. Y. Nyein, T. S. Liaw, L.-C. Tai and Q. P. Ngo, ACS Nano, 2018, 12, 6978–6987.
32 J. Zhao, Y. Lin, J. Wu, H. Y. Y. Nyein, M. Bariya, L.-C. Tai, M. Chao, W. Ji, G. Zhang and Z. Fan, ACS Sens., 2019, 4, 1925–1933.
33 W. Gao, S. Emaminejad, H. Y. Y. Nyein, S. Challa, K. Chen, A. Peck, H. M. Fahad, H. Ota, H. Shiraki and D. Kiriya, Nature, 2016, 529, 509–514.
34 H. Hojaiji, Y. Zhao, S. Lin, M. C. Gong, M. Mallajosyula, H. Lin, A. M. Hojaiji, A. M. Madni and S. Emaminejad, J. Microelectromechanical Syst., 2020, 29, 1106–1108.
35 A. J. Bandodkar, W. Jia, C. Yardımcı, X. Wang, J. Ramirez and J. Wang, Anal. Chem., 2015, 87, 394–398.
36 B. Paul, S. Demuru, C. Lafaye, M. Saubade and D. Briand, Adv. Mater. Technol., 2021, 6, 2000910.
37 H. Li, G. Wu, Z. Weng, H. Sun, R. Nistala and Y. Zhang, ACS Sens., 2021, 6, 2181-2190.
38 J. J. García-Guzmán, C. Pérez-Ràfols, M. Cuartero and G. A. Crespo, TrAC Trends Anal. Chem., 2020, 116148.
39 M. Parrilla, M. Cuartero, S. Padrell Sánchez, M. Rajabi, N. Roxhed, F. Niklaus and G. A. Crespo, Anal. Chem., 2018, 91, 1578–1586.
40 S. Mitragotri, M. Coleman, J. Kost and R. Langer, J. Appl. Physiol., 2000, 89, 961-966.
41 P. P. Samant, M. M. Niedzwiecki, N. Raviele, V. Tran, J. Mena-Lapaix, D. I. Walker, E. I. Felner, D. P. Jones, G. W. Miller and M. R. Prausnitz, Sci. Transl. Med., 2020, 12, eaaw0285.

Published on 07 March 2022. Downloaded by University College Cork on 3/8/2022 3:24:05 PM.

Lab on a Chip Accepted Manuscript

View Article Online
DOI: 10.1039/D2LC00183G

42 G. Rao, P. Glikfeld and R. H. Guy, *Pharm. Res.*, 1993, **10**, 1751–1755.
43 C. McCormick, D. Heath and P. Connolly, *Sens. Actuators B Chem.*, 2012, **166**, 593–600.
44 B. Leboulanger, R. H. Guy and M. B. Delgado-Charro, *Eur. J. Pharm. Sci.*, 2004, **22**, 427–433.
45 Y. Yao, J. Chen, Y. Guo, T. Lv, Z. Chen, N. Li, S. Cao, B. Chen and T. Chen, *Biosens. Bioelectron.*, 2021, **179**, 113078.
46 M. Tierney, H. Kim, M. Burns, J. Tamada and R. Potts, *Electroanal. Int. J. Devoted Fundam. Pract. Asp. Electroanal.*, 2000, **12**, 666–671.
47 Y. Chen, S. Lu, S. Zhang, Y. Li, Z. Qu, Y. Chen, B. Lu, X. Wang and X. Feng, *Sci. Adv.*, 2017, **3**, e1701629.
48 E. De la Paz, A. Barfidokht, S. Rios, C. Brown, E. Chao and J. Wang, *Anal. Chem. 2021* **93**, 12767-12775.
49 H. Y. Y. Nyein, W. Gao, Z. Shahpar, S. Emaminejad, S. Challa, K. Chen, H. M. Fahad, L.-C. Tai, H. Ota and R. W. Davis, ACS Nano, 2016, 10, 7216–7224.
50 J. Kim, J. R. Sempionatto, S. Imani, M. C. Hartel, A. Barfidokht, G. Tang, A. S. Campbell, P. P. Mercier and J. Wang, Adv. Sci., 2018, 5, 1800880.
51 J. R. Sempionatto, M. Lin, L. Yin, K. Pei, T. Sonsa-ard, A. N. de Loyola Silva, A. A. Khorshed, F. Zhang, N. Tostado and S. Xu, Nat. Biomed. Eng., 2021, 1–12.
52 J. Choi, S. Chen, Y. Deng, Y. Xue, J. T. Reeder, D. Franklin, Y. S. Oh, J. B. Model, A. J. Aranyosi and S. P. Lee, Adv. Healthc. Mater., 2021, 10, 2000722.
53 R. Ghaffari, D. S. Yang, J. Kim, A. Mansour, J. A. Wright Jr, J. B. Model, D. E. Wright, J. A. Rogers and T. R. Ray, ACS Sens., 2021, 6, 2787–2801.
54 A. Rimessi, V. A. Vitto, S. Patergnani and P. Pinton, *Front. Pharmacol.*, 2021, **12**, 166.
55 J. Forstner and G. Forstner, *Pediatr. Res.*, 1976, **10**, 609–613.
56 I. Oliynyk, G. Varelogianni, G. M. Roomans and M. Johannesson, *Apmis*, 2010, **118**, 982–990.
57 R. J. Feigal and B. L. Shapiro, *Pediatr. Res.*, 1979, **13**, 764–768.
58 S. B. Kim, K. Lee, M. S. Raj, B. Lee, J. T. Reeder, J. Koo, A. Hourlier-Fargette, A. J. Bandodkar, S. M. Won and Y. Sekine, Small, 2018, 14, 1802876.
59 J. Xu, Z. Zhang, S. Gan, H. Gao, H. Kong, Z. Song, X. Ge, Y. Bao and L. Niu, ACS Sens., 2020, 5, 2834–2842.
60 H. Nose, G. W. Mack, X. Shi and E. R. Nadel, J. Appl. Physiol., 1988, 65, 318–324.
61 S. Fortney, C. Wenger, J. Bove and E. Nadel, J. Appl. Physiol., 1983, 55, 884–890.
62 M. Parrilla, I. Ortiz-Gómez, R. Canovas, A. Salinas-Castillo, M. Cuartero and G. A. Crespo, Anal. Chem., 2019, 91, 8644–8651.
63 J. Madden, C. O'Mahony, M. Thompson, A. O'Riordan and P. Galvin, Sens. Bio-Sens. Res., 2020, 29, 100348.

Published on 07 March 2022. Downloaded by University College Cork on 3/8/2022 3:24:05 PM.

Lab on a Chip Accepted Manuscript

This journal is © The Royal Society of Chemistry 20xx